J Radioanal Nucl Chem (2015) 304:1001–1008
DOI 10.1007/s10967-015-3944-5

Neutron spectrometry and determination of neutron contamination around the 15 MV Siemens Primus LINAC

Najmeh Mohammadi · Hashem Miri-Hakimabad · Laleh Rafat-Motavlli · Fatemeh Akbari · Sara Abdollahi

Received: 21 July 2014 / Published online: 20 January 2015

Abstract Despite the importance of photoneutrons doses produced in the high-energy linear accelerators, currently they are not considered in the treatment planning systems. Therefore, it is necessary to characterize the photoneutrons produced around the linacs. For this purpose, the main components of head of 15 MV Siemens Primus were simulated using MCNPX 2.6. Neutron contamination was calculated in the treatment room at the isocenter. The maximum dose equivalent of neutrons was found in 25 cm × 25 cm field size. Neutron spectrum was also measured applying the Bonner sphere with gold foils and artificial neural network as unfolding method.

Keywords Neutron contamination · Bonner sphere spectrometry · High-energy linac · Monte Carlo

Introduction

Radiotherapy with photon beams still represents the most spread technique to control and kill tumor cells [1]. Recently, the high-energy medical linear accelerators (linacs) operated above 10 MV are widely utilized to eliminate tumor cells. In this procedure, electron beam is directed to strike a target, normally made of high-Z materials like tungsten or gold, and Bremsstrahlung photons are produced inside the linac's head. In addition to required photon, linacs also produce undesirable particles such as neutrons, which raise concerns about radiation dose due to the high ranges and high LETs of their interaction products [2].

The main components of the linac's head such as target, collimators, and flattening filter constructed from materials like Au, W, Al, Fe, and Pb as well as the element concentration in treatment room, couch and patient body, like C, H, O, N, S, and Mg have a threshold energy to produce neutrons through (γ, n) interaction, which are referred to as photoneutrons [3]. The threshold energy of some isotopes for the (γ, n) reaction were listed in the Table 1. Photoneutrons pass through the shield of linac's head, scatter throughout the treatment vault, and may ultimately deposit their energies in the patient. Therefore, to evaluate the possibility of subsequent cancer risk, the photoneutron doses should be specified accurately.

In the current treatment planning systems, the photoneutrons are not transported while many researchers are interested to calculate the photoneutron dose around the high-energy linacs because of the importance of photoneutron effects on the patient body. With advances in computational codes, it is possible to track the produced photoneutrons and calculate the undesirable doses received by patients. However, before calculating the photoneutron doses in the human phantom, we must ensure that the simulated model is correct and Monte Carlo calculation is accurate.

Several works were done about the neutron contaminations around the high-energy linac for various types and energy of linacs [5–7]. These studies were done with different computational codes such as GEANT4 [8] and MCNPX [2, 9], or different methods of measurements such as Bobble detector [10, 11], TLD [12, 13] and Nuclear Track detectors [14, 15]. In this study was tried to validate the neutron calculations with experimental using the

N. Mohammadi · H. Miri-Hakimabad (✉) · L. Rafat-Motavlli
Faculty of Sciences, Ferdowsi University of Mashhad, Mashhad, Iran
e-mail: mirihakim@yahoo.com

F. Akbari · S. Abdollahi
Reza Radiation Oncology Center, Mashhad, Iran

Table 1 The threshold energy for (γ, n) reaction for different isotopes [4]

Isotope	The threshold energy for (γ, n) reaction (MeV)
^{12}C	18.27
^{14}N	10.55
^{16}O	15.66
^{32}S	15.04
^{24}Mg	16.53
^{27}Al	13.06
^{56}Fe	11.2
^{184}W	7.41
^{197}Au	8.07
^{208}Pb	7.37

Bonner spheres method for neutron spectrometry. In this method various thermal neutron detectors such as TLD [3, 16], gold foils [17], or ^{3}He proportional counters [18, 19], and different methods of unfolding such as MAXED algorithm [20], BUNKIUT [21] and FRUIT code [17] were applied. We used gold foils as thermal neutron detector and Artificial Neural Network approach [22] for unfolding the neutron spectrum around the 15 MV Siemens Primus linac at Reza Radiation Oncology Center. We assay the experimental method for further neutron contamination evaluation around the other linacs at mentioned center.

Moreover, in this work, a detailed model of 15 MV Siemens Primus linear accelerator head was simulated using the Monte Carlo method. The measured percentage depth dose (PDD) curves as well as beam profiles were compared with those obtained from calculation for model validation. In order to verify the photoneutrons calculation experimentally, the measured energy distribution of neutron by Bonner sphere system (BSS) was compared with obtained spectrum using MCNP. To evaluate the photoneutron dose, a 5-cm radius sphere of air simulated at the isocenter, and neutron dose equivalent was calculated in it for different irradiation field sizes and influence of size of irradiation field was evaluated on the neutron dose equivalent. In addition, the distribution of main component of linac's head in the photoneutron production was also calculated.

Methods and materials

Monte Carlo simulation

The MCNPX code version 2.6 [23] was used to simulate the head of 15 MV Siemens Primus medical linear accelerator based on manufacture data. The simulated geometry of the linac's head is shown in the Fig. 1. This model included the target, absorber, primary collimator, photon chamber, flattening filter, jaws (secondary collimators), and shield. The simulated components of linac's head are tabulated in Table 2.

The electron source was modeled as a 0.2-cm radius disk, which produced electrons with a Gaussian energy distribution. The optimum energy of incident electron spectrum was selected among the ±0.5 MeV energy range relative to the manufacturer-provided energy spectrum. The selection of the optimum energy was based on the agreement of build-up depth determined from Monte Carlo simulations with that of the experimental measurements.

To calculate the PDD curve and beam profiles, a water phantom with dimensions of 50 cm × 50 cm × 50 cm was simulated under the linac's head with a source-surface distance (SSD) of 100 cm. The phantom was divided into cylindrical meshes with 1 cm radius and 1 mm height, in which the deposited energy of photons and electrons were recorded using mesh tally (type 3) to calculate the relative dose absorbed in the phantom. To plot PDD curve and off-axis beam profiles (in percent), the deposited energy in each cell was divided to the maximum value. The statistical errors were less than 2 %.

The measurements of both depth dose and beam profiles were performed with a Semiflex ionization chamber (having a 0.125 cm^3 of volume) at SSD of 100 cm in the Reza Radiation Oncology Center with relative error of 1 %.

After finding the spectrum of electron source, to save time in running the programs, surface source write (SSW)/surface source read (SSR) card was used. For this, a total number of 2×10^9 electrons were tracked and 7.7×10^8 particles including electrons, photons and neutrons were recorded with their specifications (such as energy, angular distribution, and direction) below the ion chamber on horizontal plane by SSW card. For subsequent calculation, recorded particles were read by SSR card. The PHYS:P and mpn card were used to account neutron production from (γ, n) interaction. To calculate thermal neutron scattering, MT card was also used. In these simulations, uncertainties were kept below 3 %. The energy cut-off for electron and photon were assumed 0.5 and 0.01 MeV, respectively.

Neutron calculations

To find the neutron source strength (Q) of the simulated linac's head, the number of photoneutrons produced per Gy of photon dose at isocenter was calculated. For this purpose, a spherical surface with a radius of 100 cm was simulated; so that its center was located on the target according to the McGinley and Lundry method [24]. F1 and F6 tallies were used to compute the number of photoneutrons crossing the surface and absorbed dose from photons at the isocenter per initial electron, respectively.

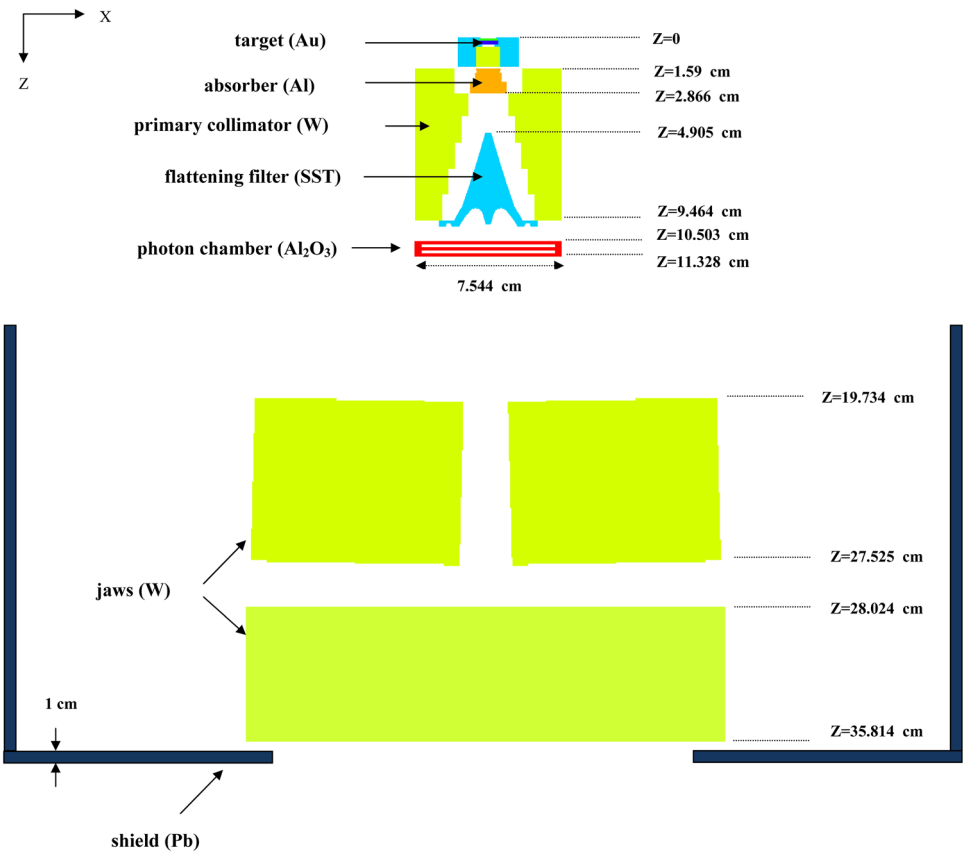

Fig. 1 Detailed geometry of simulated linac's head

Table 2 Main components of linac's head

Elements	Material
Target	Gold
Absorber	Aluminum
Flattening filter	Stainless steel alloy (SST-303)
Primary collimator	Tungsten
Photon chamber	Aluminum oxide (Al_2O_3-alumina)
Jaws	Tungsten
Shield	Lead

To calculate the photoneutron dose equivalent, the NCRP38 fluence-to-dose equivalent conversion factors were used [25]. For this, the F4 tally (flux averaged over a cell) was used and the fluence-to-dose equivalent conversion factors, which are energy depended, were entered in the input file of MCNP by dose energy (DE) and dose function (DF) cards.

The statistical error in the neutron calculation was obtained about 5 %, so the seed number in the input files of each filed size was changed and each program was repeated for five times. Consequently, the uncertainties of neutron dose was reduced with an acceptable error.

The results from the repeated calculations can be combined using a batch-statistics approach. That is, for each tally quantity X, the series of results from the repeated calculations, $\{X_k, k = 1, M\}$, where M is the number of repeated calculations, can be computed as:

$$\bar{X} = \frac{1}{M}\sum_{k=1}^{M} X_k. \quad (1)$$

The uncertainty in the average of a scored quantity, X, to be:

$$\sigma_{\bar{X}} = \sqrt{\frac{\sum_{k=1}^{M}(X_k - \bar{X})^2}{M(M-1)}}, \quad (2)$$

where N is the number of batches, X_k is the value of X in batch k, and $\bar{X}$ is the mean value of X evaluated over all batches [26, 27].

In order to calculate the photoneutron production contribution of different components of linac's head, the photoneutron production was only considered in the desired component such as primary collimator, flattening filter, jaws, and lead shielding. That is the mpn card was considered zero for other components. Then, the obtained values were divided to total number of produced photoneutrons, which is generated from all of components. Therefore, the neutron production percentages were calculated for desired components. It should be mentioned

that, in the neutron calculations, to save the running time the energy cut-off for electrons and photons was assumed 7 MeV, below the photonuclear interaction.

Measurements of neutron spectrum

Neutron dose is highly dependent on energy, so the neutron spectrometry is necessary for neutron dosimetry. However, neutron dosimetry is not an easy task because of the type of its interactions with matter. Nevertheless, neutron spectrometry using Bonner sphere is a conventional method, which covers a wide energy range from thermal up to several of MeV. Around the linacs the radiation field is mixed, pulsed and intense inducing pulse pileup and large dead times in active neutron detectors, to overcome this drawback passive detectors are used, like thermoluminescent dosimeters [21]. Here, neutron spectrometry was performed using Bonner sphere spectrometer with gold foils as thermal neutron detectors. This procedure was done using a series of seven high-density polyethylene $\left(\rho = 0.95\ {}^{\mathrm{g}}/_{\mathrm{cm}^3}\right)$ moderating spheres ranging from 3.5 to 12 inches in diameter surrounding a passive thermal neutron detector placed at the center of the each sphere. In this study, ^{197}Au foils were used as passive detectors inside the treatment vault. ^{197}Au primarily has a large absorption cross section for thermal neutrons.

The saturation activity, in Bq/g, of each foil at the end of the irradiation was calculated using following equation [18, 28]:

$$A_{\infty_i} = \frac{\lambda t_{\mathrm{m}} C}{mq\varepsilon} \frac{\mathrm{e}^{\lambda t_w}}{(1-\mathrm{e}^{-\lambda t_{\mathrm{i}}})(1-\mathrm{e}^{-\lambda t_{\mathrm{m}}})}, \tag{3}$$

where λ is the decay constant of ^{198}Au (2.97×10^{-6} per second), m is the mass of Au foil (in term of g), q is its branching ratio (0.995), C is the net area at 411 keV photo-peak after background and dead time corrections, ε is the detector efficiency calculated by MCNPX which was obtained 0.2 [29], t_{m}, t_{i} and t_{w} are the measurement, irradiation and elapsed time between irradiation and measurement time period, respectively.

On the other hand, the activities of gold foils could be obtained from Eq. 4 [30, 31];

$$A_{\infty_i} = \sum_{j=1}^{N} R_{ij}(E)\Phi_j(E)\Delta E_j, \tag{4}$$

where $R_{ij}(E)$ is the response function of ith BS and $\Phi_j(E)$ is the neutron fluence in the energy of E_j. To find the neutron spectrum, an unfolding method is needed. For this purpose, we used the response matrix, which was simulated and verified in our previous study for ^{241}Am-Be source [29].

To measure the photoneutron spectrum produced in the linac's head each BS was placed at the isocenter of the treatment room and was irradiated for 600 cGy, with dose rate of 200 MU/min, in the 15 cm × 15 cm irradiation field size at Reza Radiation Oncology Center. For the 10 cm × 10 cm irradiation filed, 1 MU = 1 cGy at the isocenter. The experimental setup is shown in the Fig. 2. To avoid neutron scattering from the couch, an iron bar and wooden box were placed above it. The wooden box was with length, width, and height of 50, 40, and 30 and with 1.5 cm-thick. The bar iron was also with length of 80 and 1 cm-diameter which was set at the center of wooden box. In this setup, the BS was not in direct contact with couch, and our calculations showed that with this setup the neutron scattering from the couch decreased about 50 %. After irradiation of each sphere, the photo-peak of 411 keV γ-ray emitting from active gold foil was measured using $3'' \times 3''$ NaI(Tl) detector in a counting time of 3–4 h. The detector was calibrated with standard sources include the ^{137}Cs, ^{60}Co, and ^{22}Na. To shield the detector from the background gamma, the lead blocks were placed around the detector. In addition, the background spectrum was subtracted from the measured gamma spectra of the active gold foils for background correction. After calculation of the foil activities, the neural network unfolding method was employed using the nntool of matlab 2012a software [22].

Fig. 2 Irradiation of Bonner sphere with 15 MV linac

Results and discussion

PDD curve and beam profiles

The comparisons between calculated and measured PDD curves are displayed in Fig. 3. According to the results, two curves are consistent with each other with differences less than 2 % except in the build-up region. After the build-up region, the differences between calculations and measurements are in their error range, which are acceptable. However, there are meaning differences in the build-up

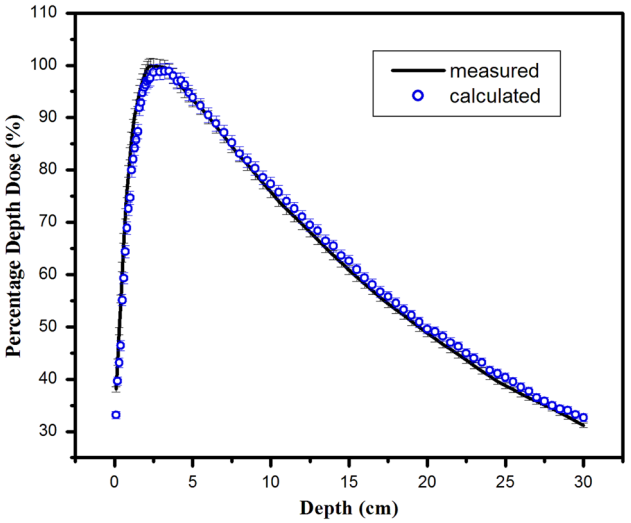

Fig. 3 Calculated and measured PDD for 15 MV linac for 10 cm × 10 cm field size

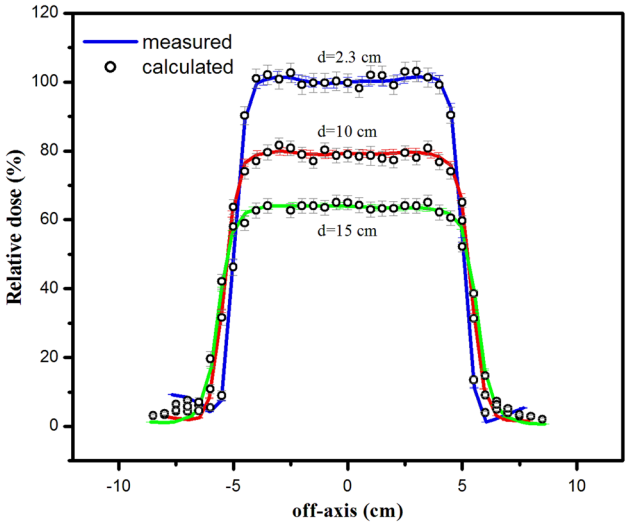

Fig. 4 Calculated and measured beam profiles at depths of 2.3, 10, and 15 cm for 10 cm × 10 cm field size

Table 3 Calculated and measured data of PDD at depths of 3 and 4 cm (%) and D_{20}/D_{10}, which is the ratio of depth doses on the central axis, at 20 and 10 cm, respectively

	3 cm (%)	4 cm (%)	D_{20}/D_{10}
Measurement	99.8 ± 1.4	97.1 ± 1.4	0.64 ± 0.01
Calculation	98.5 ± 1.5	97.08 ± 1.5	0.66 ± 0.01

region. It is due to a high gradient of dose distribution in that region, which makes ionization chamber measurements unreliable. Also, finite size of the ionization chamber, which perturbs the absorbed dose, may be another reason for their large local differences [32].

The measured and calculated values of relative dose at depths of 3 and 4 cm, and ratio of deposited energy at depths of 20–10 cm (D_{20}/D_{10}) are compared in the Table 3. According to the Table 3, there is a good agreement between the results of experiments and simulations.

Beam profile was determined at different depths of 2.3, 10, and 15 cm in the water phantom. The measured and calculated results for 10 cm × 10 cm field size are presented in Fig. 4. From this figure, the differences between the results is less than 3 %, which is in the acceptable deviation limit [33]. Given this accordance, the simulation of linac's head is verified.

Neutron spectrum

To obtain neutron spectrum, artificial neural network (ANN) method was used for unfolding [34–36]. The measured and calculated spectra, per 1 Gy photon absorbed dose at isocenter, are compared in the Fig. 5. There are two peaks in the measured spectrum, one for thermal neutrons and

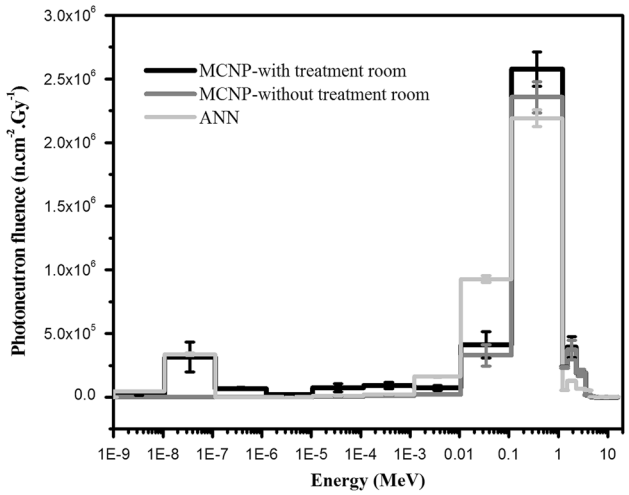

Fig. 5 Calculated and measured neutron spectra for 15 MV linac at isocenter for 15 cm × 15 cm irradiation field

another for fast neutrons between 0.5 and 1.5 MeV, this peak is the "signature" of evaporation neutrons [37, 38], while thermal and epithermal neutrons are due to neutrons leaking-out the linacs' head, scattered by couch, floor and walls of treatment room [39, 40]. Two calculated spectra were also displayed in this figure. The results showed that the neutron spectrum calculated without considering the treatment room has the peak at the fast area. This means that the photoneutrons originated from the linac's head has only the fast component. While by considering the treatment room (including floor, ceiling, and walls made of concrete and couch composited of plastic), based on the treatment room of Reza Radiation Oncology Center, the thermal peak of photoneutrons was also observed. This outcome indicated that neutrons scatter form the components of treatment

Table 4 The value of ND1, ND2, Q, and neutron production from jaws for different field sizes

	10 × 10 cm^2	15 × 15 cm^2	20 × 20 cm^2	25 × 25 cm^2	30 × 30 cm^2	35 × 35 cm^2	40 × 40 cm^2
ND1 (mSv/Gy)	0.86 ± 0.01	1.09 ± 0.02	1.16 ± 0.02	1.23 ± 0.02	1.19 ± 0.02	1.09 ± 0.02	1.1 ± 0.02
ND2 (mSv/Gy)	0.88 ± 0.02	1.16 ± 0.02	1.27 ± 0.02	1.32 ± 0.02	1.3 ± 0.02	1.23 ± 0.02	1.14 ± 0.02
Neutron production in jaws (%)	29.7 ± 0.05	28 ± 0.05	25.6 ± 0.05	22.6 ± 0.05	18.7 ± 0.05	14.1 ± 0.05	9.1 ± 0.05

room, and lose their energies and then form the thermal peak [41, 42].

In both measured and calculated neutron spectra, the peak of fast neutron is in the energy range of evaporation neutrons. Based on ICRP 103 (International Commission on Radiological Protection), radiation weighting factors have their maximum values in this neutron energy range. Therefore, in this condition, harmful effects of neutrons in the patient body are in the high degree [43].

Neutron contamination

As mentioned, the different parts of linac head are composed from heavy elements. To find the most influential component in neutron contamination, the contribution of major parts of linac head in neutron production were evaluated. Our calculation showed that the largest neutron production occurs in the primary collimator. So that the neutron production of components such as primary collimator, flattening filter, jaws, and lead shielding was 66, 2, 28, and 3 %, respectively for 15 cm × 15 cm irradiation field size. Then we evaluated the effect of opening angle of jaws on neutron production at the isocenter for seven irradiation field sizes ranging from 10 cm × 10 cm to 40 cm × 40 cm. These results indicated that by increasing the field size, the contribution of jaws decreased because the photons interactions with jaws were reduced (Table 4).

Using mentioned method to calculate the neutron strength, a total number of photoneutrons per 1 Gy of photon dose was obtained for different field sizes, which the average value of Q of 0.19 × 10^{12} nGy^{-1} was agreed to the value reported by Lin et al. (0.2 × 10^{12} nGy^{-1}) [44].

The measured spectrum of neutron at isocenter for 15 cm × 15 cm field size was folded by the fluence-to-dose conversion factors of NCRP38, and neutron dose equivalent was calculated as 1 ± 0.03 mSv/Gy. This value is comparable with calculated value of 1.16 ± 0.02 mSv/Gy. This difference in the energy range of 0.03–0.4 MeV in the calculated and measured neutron spectra (Fig. 5), did not make a huge variation in the amount of neutron dose equivalent, because the value of fluence-to-dose conversion factors in this energy range is much lower than of 0.5–1.5 MeV.

Moreover, to find the treatment room effect on neutron dose equivalent, this parameter was calculated at the isocenter without (ND1) and with (ND2) considering the

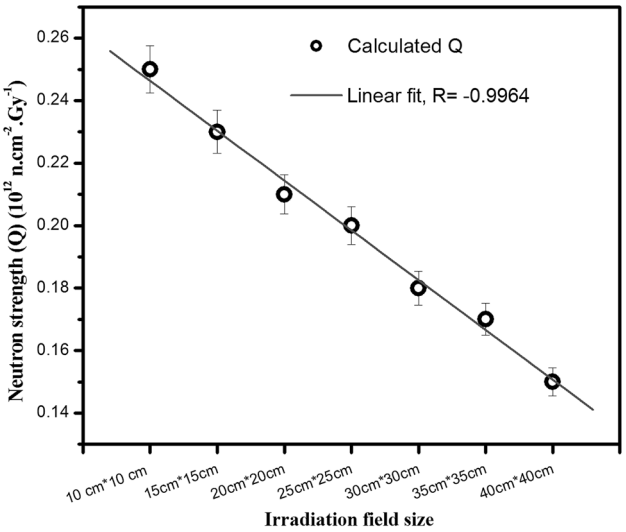

Fig. 6 The neutron strength (Q) as a function of irradiation field size

treatment room in the MCNP simulation, as listed in the Table 4. It should be note that the photoneutron production from the wooden box and bar iron was less than 0.001 %. So these items were not considered in the simulations.

Based on the obtained outcomes, considering the treatment room and the neutron scattering contribution, slightly increased the value of neutron dose equivalent. This means that the thermal neutrons had small contribution on neutron dose, and the fast neutrons had the largest influence on the neutron dose equivalent. The calculations showed that the more than of 90 % of neutron dose equivalent was corresponded to fast neutrons with energy above 0.5 MeV.

The Fig. 6 shows the variation of neutron strength (Q) as the function of the irradiation field size. The results showed that, as the field size increases the value of Q decreases linearly, with regression of $R = -0.9964$, because there is less material in the beam shaping devices (jaws) being presented to the Bremsstrahlung beam. The similar results were obtained by Mao and Ma [1, 45].

However, the neutron dose equivalent for different irradiation field sizes has not changed like Q. For find the reason of this behavior, the fast neutron fluence (with energy above 0.5 MeV) as a function of irradiation field size was plotted in the Fig. 7. It is seen that the trend of the neutron dose equivalent is similar to the fast neutrons. This fact is due to

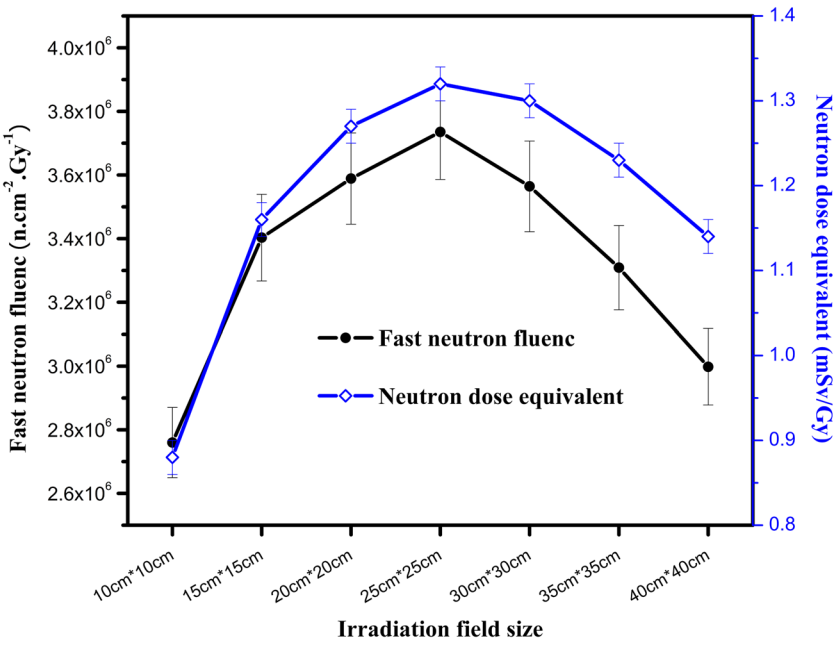

Fig. 7 Fast neutrons fluence and neutron dose equivalent for different irradiation field sizes

the major role of fast neutrons in the neutron dose equivalent. The results showed that 25 cm × 25 cm field has the largest value of fast neutron fluence among the other field sizes. This led to maximum neutron dose equivalent in the 25 cm × 25 cm field due to high influence of fast neutrons on the dose equivalent. This outcome was similar to the KIM report [46], which the 20 cm × 20 cm field size have the maximum dose in the Varian Clinac 2100C/2300C medical accelerator.

Conclusion

In this study, the geometry of 15 MV Siemens Primus head was modeled using MCNPX code. The calculated PDD curves and beam profiles were compared with those obtained by measurements. Considering the good agreements between the results, model simulation was verified. BS with gold foil (as thermal neutron detector) was used to determine photoneutron spectrum, which was unfolded by ANN method. From the measurement and calculation, a peak of 0.5–1.5 MeV was observed in photoneutron spectrum. Considering the high value of radiation weighting factor of neutrons with this energy range, the damages to the patient body increases.

To evaluate the contamination of photoneutrons during the radiotherapy with high-energy linac, the dose equivalent of photoneutron was calculated at the isocenter for different irradiation field sizes. Considering the results, the largest dose was obtained for 25 cm × 25 cm irradiation field size.

References

1. Ma A, Awotwi-Pratt J, Alghamdi A, Alfuraih A, Spyrou NM (2008) Monte Carlo study of photoneutron production in the VarianClinac 2100C linac. J Radioanal Nucl Chem 276:119–123
2. Pena J, Franco L, Gomez F, Iglesias A, Pardo J, Pombar M (2005) Monte Carlo study of Siemens PRIMUS photoneutron production. Phys Med Biol 50:5921–5933
3. Vega-Carrillo HR, Hernandez-Almaraz B, Hernandez-Davila VM, Ortiz-Hernandez A (2010) Neutron spectrum and doses in a 18 MV LINAC. J Radioanal Nucl Chem 283:261–265
4. Chadwick MB, Oblozinsky P, Blokhin A, Fukahori T, Han Y, Lee YO, Martins MN, Mughabghab SF, Varlamov VV, Yu B (2000) Handbook on photonuclear data for applications: cross sections and spectra. IAEA TECH-DOC 1178
5. Garnica-Garza HM (2005) Characteristics of the photoneutron contamination present in a high-energy radiotherapy treatment room. Phys Med Biol 50:531–539
6. Martinez-Ovalle SA, Barquero R, Gomez-Ros JM, Lallena AM (2012) Ambient neutron dose equivalent outside concrete vault rooms for 15 and 18 MV radiotherapy accelerators. Radiat Prot Dosim 148:457–464
7. Carinou E, Stamatelatos IE, Kamenopoulou V, Georgolopoulou P, Sandilos P (2005) An MCNP-based model for the evaluation of the photoneutron dose in high energy medical electron accelerators. Phys Med 21:95–99
8. Saeed MK, Moustafa O, Yasin OA, Tuniz C, Habbani FI (2009) Doses to patients from photoneutrons emitted in a medical linear accelerator. Radiat Prot Dosim 133:130–135
9. Vega-Carrillo HR, Martinez-Ovalle SA, Lallena AM, Mercado GA, Benites-Rengifo JL (2012) Neutron and photon spectra in LINACs. Appl Radiat Isot 71:75–80
10. Ongaro C, Zanini A, Nastasi U, Rodenas J, Ottaviano G, Manfredotti C (2000) Analysis of photoneutron spectra produced in medical accelerators. Phys Med Biol 45:55–61
11. Lin JP, Liu WC, Lin CC (2007) Investigation of photoneutron dose equivalent from high-energy photons in radiotherapy. Appl Radiat Isot 65:599–604

12. Hsu FY, Chang YL, Liu MT, Huang SS, Yu CC (2010) Dose estimation of the neutrons induced by the high energy medical linear accelerator using dual-TLD chips. Radiat Meas 45:739–741
13. Mukherjee B, Makowski D, Simrock S (2005) Dosimetry of high-energy electron linac produced photoneutrons and the bremsstrahlung gamma-rays using TLD-500 and TLD-700 dosimeter pairs. Nucl Instrum Methods Phys Res A 545:830–841
14. Alem-Bezoubiri A, Bezoubiri F, Badreddine A, Mazrou H, Lounis-Mokrani Z (2014) Monte Carlo estimation of photoneutrons spectra and dose equivalent around an 18MV medical linear accelerator. Radiat Phys Chem 97:381–392
15. Al-Ghamdi H, Al-Jarallah MI, Maalej N (2008) Photoneutron intensity variation with field size around radiotherapy linear accelerator 18-MeV X-ray beam. Radiat Meas 43:S495–S499
16. Barquero R, Mendez R, Vega-Carrillo HR, Iniguez MP, Edwards TM (2005) Neutron spectra and dosimetric features around an 18 MV linac accelerator. Health Phys 88:48–58
17. Domingo C, Garcia-Fuste MJ, Morales E, Amgarou K, Terron JA, Rosello J, Brualla L, Nunez L, Colmenares R, Gomez F (2010) Neutron spectrometry and determination of neutron ambient dose equivalents in different LINAC radiotherapy rooms. Radiat Meas 45:1391–1397
18. Barros S, Mares V, Bedogni R, Reginatto M, Esposito A, Goncalves IF, Vaz P, Ruhm W (2014) Comparison of unfolding codes for neutron spectrometry with Bonner spheres. Radiat Prot Dosim 161:46–52
19. Garny S, Mares V, Roos H, Wagner FM, Ruhm W (2011) Measurement of neutron spectra and neutron doses at the Munich FRM II therapy beam with Bonner spheres. Radiat Meas 46:92–97
20. Howell RM, Kry SF, Burgett E, Hertel NE, Followill DS (2009) Secondary neutron spectra from modern Varian, Siemens, and Elekta linacs with multileaf collimators. Med Phys 36:4027–4038
21. Vega-Carrillo HR, Ortiz-Hernandez A, Hernandez-Davila VM, Hernandez-Almaraz B, Montalvo TR (2010) H*(10) and neutron spectra around linacs. J Radioanal Nucl Chem 283:537–540
22. Demuth H, Beale M (2002) Neural network toolbox for use with MATLAB, User guide version 4. (The MathWorks, Inc.)
23. Pelowitz DB (2008) MCNPXTM user's manual, Version 2.6.0. Los Alamos National Laboratory Report LA-CP- 07-1473
24. McGinley PH, Landry JC (1989) Neutron contamination of X-ray beams produced by the Varian Clinac 1800. Phys Med Biol 34:777–783
25. NCRP 38 (1971) Protection against neutron radiation, National Council on Radiation and Protection and Measurement
26. Brown FB, Sweezy JE, Hayes R (2004) Monte Carlo parameter studies and uncertainty analyses with MCNP5. PHYSOR-2004. In: American nuclear society reactor physics topical meeting
27. Walters BRB, Kawrakow I, Rogers DWO (2002) History by history statistical estimators in the BEAM code system. Med Phys 29:2745–2752
28. Ortiz-Rodriguez JM, Reyes Alfaro A, Reyes Haro A, Cervantes Viramontes JM, Vega-Carrillo HR (2014) A neutron spectrum unfolding computer code based on artificial neural networks. Radiat Phys Chem 95:428–431
29. Mohammadi N, Motavalli LR, Hakimabad HM (2014) Neural network unfolding of neutron spectrum measured by gold foil-based Bonner sphere. J Radioanal Nucl Chem. doi:10.1007/s10967-014-3650-8
30. Amgarou K, Lacoste V, Muller H, Fernandez F (2007) Set-up of a passive Bonner sphere system for neutron spectrometry at mixed fields with predominant photon component based on activation detector. Radiat Prot Dosim 126:337–341
31. Fernandez F, Bouassoule T, Amgarou K, Domingo C, Garcia MJ, Lacoste V, Gressier V, Muller H (2007) Monte Carlo calculations and validation of a gold foil-based Bonner sphere system. Radiat Prot Dosim 126:366–370
32. Siebers JV, Keall PJ, Libby B, Mohan R (1999) Comparison of EGS4 and MCNP4b Monte Carlo codes for generation of photon phase space distributions for a Varian 2100C. Phys Med Biol 44:3009–3026
33. Wieslander E, Knoos T (2000) A virtual linear accelerator for verification of treatment planning systems. Phys Med Biol 45:2887–2896
34. Sharghi Ido A, Bonyadi MR, Etaati GR, Shahriari M (2009) Unfolding the neutron spectrum of a NE213 scintillator using artificial neural networks. Appl Radiat Isot 67:1912–1918
35. Claudia CB, Mauro SD (2002) Application of neural networks for unfolding neutron spectra measured by means of Bonner spheres. Nucl Instrum Methods Phys Res A 476:252–255
36. Vega-Carrillo HR, Hernandez-Davila VM, Manzanares-Acuna E, Gallego E, Lorente A, Iniguez MP (2007) Artificial neural networks technology for neutron spectrometry and dosimetry. Radiat Prot Dosim 126:408–412
37. Facure A, Falcao RC, da Silva AX, Crispim VR, Vitorelli JC (2005) A study of neutron spectra from medical linear accelerators. Appl Radiat Isot 62:69–72
38. Vega-Carrillo HR, Baltazar-Raigosa A (2011) Photoneutron spectra around an 18 MV LINAC. J Radioanal Nucl Chem 287:323–327
39. Vega-Carrillo HR, Rivera-Perez E (2014) Moderator for neutron activation with the photoneutrons produced by a LINAC. J Radioanal Nucl Chem 299:1499–1507
40. Kry SF, Salehpour M, Followill DS, Stovall M, Kuban DA, White RA, Rosen II (2005) Out-of-field photon and neutron dose equivalents from step-and-shoot intensity-modulated radiation therapy. Int J Radiat Oncol Biol Phys 62:1204–1216
41. dErrico F, Luszik-Bhadra M, Nath R, Siebert BRL, Wolf U (2001) Depth dose-equivalent and effective energies of photoneutrons generated by 6-18 MV X-ray beams for radiotherapy. Health Phys 80:4–11
42. Gonzalez-Soto X, Amgarou K, Lagares JI, Exposito MR, Gomez F, Domingo C, Sanchez-Nieto B, Sanchez-Doblado F (2013) Neutron distribution in radiotherapy treatment rooms. World Congr Med Phys Biomed Eng IFMBE Proc 39:1245–1248
43. ICRP 103 (2007) Recommendations of the international commission on radiological protection. Ann ICRP 37:2–3
44. Lin JP, Chu TC, Lin SY, Liu MT (2001) The measurement of photoneutrons in the vicinity of a Siemens Primus linear accelerator. Appl Radiat Isot 55:315–321
45. Mao XS, Kase KR, Liu JC, Nelson WR, Kleck JH, Johnsen S (1997) Neutron sources in the varian clinac 21000/23000 medical accelerator calculated by the egs4 code. Health Phys 72:524–529
46. Kim HS, Lee JK (2007) Assessment and measurement of the photoneutron field produced in the varian medical linear accelerator. J Nucl Sci Tec 44:95–101